ISSN 2411-3336; e-ISSN 2541-9404

JOURNAL OF MINING INSTITUTE
Zapiski Gornogo instituta
Journal homepage: pmi.spmi.ru

Research article Geology

Isomorphic capacity of combustion metamorphic melilite solid solutions

Ella V. Sokol, **Anna S. Polovykh**✉, **Svetlana N. Kokh**, **Ivan S. Karputin**, **Olga A. Kozmenko**
V.S.Sobolev Institute of Geology and Mineralogy SB RAS, Novosibirsk, Russia

***How to cite this article*:** Sokol E.V., Polovykh A.S., Kokh S.N., Karputin I.S., Kozmenko O.A. Isomorphic capacity of combustion metamorphic melilite solid solutions. Journal of Mining Institute. 2026. Vol. 280, p. 70-84.

Abstract
Partitioning of trace elements between minerals crystallized from Ca-rich Si-undersaturated melts is constrained for the first time in samples of coarse combustion metamorphic (CM) melt rocks (paralavas) from the Hatrurim Formation. The partition coefficients of trace elements (including REE) in wollastonite, rankinite, cuspidine, Ti-andradite, melilite solid solutions, kalsilite, and fluorapatite are calculated on the basis of their contents determined by laser ablation inductively coupled plasma mass spectrometry (LA-ICP-MS). Most of REE are hosted by fluorapatite (≤ 900 ppm ΣREE), garnet (≤ 600 ppm), and cuspidine (≤ 300 ppm), while other phases contain < 100 ppm of total REE. Sr is found in all minerals except garnet, with its contents reaching 7500 ppm in melilite, 5500 ppm in fluorapatite, 4500 ppm in rankinite, 2150 ppm in wollastonite, 2000 ppm in cuspidine, and 800 ppm in kalsilite. High-field strength elements (HFSE) occur in cuspidine (up to 2100 ppm U, 1600 ppm Zr, 1300 ppm Ti, and 200 ppm Nb) and garnet (up to 3000 ppm Zr, 600 ppm Y, 350 ppm HREE and Sc, and 130 ppm Nb). Melilite is the principal host of Zn (≤ 17,000 ppm), Ni (≤ 2100), Cu (≤ 1200), Mn (≤ 750), Co (≤ 100), and Ga (≤ 65). It also bears Ba (up to 5500 ppm), while the amount of Ba reaches 8500 ppm in kalsilite, along with ≤ 1350 Rb. The partition coefficients of trace elements for all listed minerals were calculated. Isomorphic substitutions in melilite are controlled by structural positions at three sites (Ca, T1, and T2) which can accommodate Na, Sr, and Ba (Ca); Zn, Co, Ni, Cu (T1); Fe^{3+}, and Ga (T2). Melilite crystallized from CM melts lacks significant amounts of REE and HFSE. The obtained partition coefficients of trace elements in CM melilite are consistent with the available estimates for minerals from igneous alkaline complexes and thus have implications for trace element partitioning in Ca-rich Si-undersaturated melts. The partitioning patterns of trace elements during the crystallization of CM melts mainly depend on the crystal chemistry of minerals.

Keywords
melilite; garnet; cuspidine; kalsilite; LA-ICP-MS; trace elements; partition coefficients; paralavas; Hatrurim Formation

Funding
The study was supported by the Russian Science Foundation grant N 24-77-00014, https://www.rscf.ru/project/24-77-00014/.

Received: 23.12.2025 ***Accepted: 28.04.2026*** ***Online: 21.07.2026*** ***Published: 10.09.2026***

Introduction

Recent progress in microanalytical tools, such as mass spectrometry with secondary ions (SIMS) or laser ablation inductively coupled plasma mass spectrometry (LA-ICP-MS), allows using trace element patterns in rock-forming and accessory minerals as informative petrogenetic proxies for meteoritic material [1, 2], igneous [3-5], and metamorphic [6] rocks.

Minerals of the melilite group have been a focus of interest for igneous petrology, meteorite studies, and experimental work due to their large *P-T* stability field and high isomorphic capacity. These features facilitate isomorphic substitutions making the melilite-group minerals highly adaptive to changing conditions. The structure of melilite can accommodate more than twenty elements in considerable amounts. Melilite belongs to space group $P4\bar{2}_1m$; with the general formula

*X*T1(T2)$_2$O$_7$), where *X* stands for Ca, Na, Sr, Ba, Pb, Y, and REE, while T1 and T2 correspond to Mg, Al, Mn, Fe^{2+}, Fe^{3+}, Zn, Co, Cu, Cd (T1) and Si, Al, Fe^{3+}, Ti, B, Be, Ga, Ge (T2). The structural type is used as a framework to synthesize compounds involving Be, B, Ga, Ge, Co, Ni, Cd, Zn, Sr, Ba, and REE, which impart valuable technological properties to ferrimagnetic, ferroelectric, and ferroelastic materials. The melilite structure is strongly anisotropic (till divergent lattice distortion along *a* and *c* directions), which reduces thermal expansion of melilite-based ceramic and composite materials and substituted derivatives [7].

Most of petrological research commonly deals with melilite from igneous rocks, such as ultramafic alkaline nephelinite [4, 5, 8], melilitite [8-10], and carbonatite [11-13]) complexes, or from primitive chondrite [14-16]. Meanwhile, petrogenetic reconstructions for such rocks are difficult because magmatic melilite is compositionally complex ($Ca_2MgSi_2O_7$–$NaCaAlSi_2O_7$ solid solutions with variable contents of the $Ca_2Fe^{2+}Si_2O_7$ and $Ca_2Al_2SiO_7$ endmembers) and can be involved in peritectic reactions. Only few studies have addressed the fractionation of trace elements during the crystallization of melilite-bearing igneous rocks. Those studies have revealed considerable difference in the partitioning patterns of impurities between coexisting silicates, as well as between melilite and melt in the case of early crystallization of perovskite, apatite, titanite, loparite, and other hosts of Sr, Zr, Hf, Nb, Ta, Th, U, and REE [3, 17, 18]. Melilite was mainly investigated in high-temperature skarn [19, 20], contact metamorphic [21-23], and combustion metamorphic rocks from the Hatrurim Formation [24-26], as well as in coal-fire buchites from the Buffalo complex (Wyoming) [27], paralavas from the Central Apennines (Italy) [28], and the Khamaryn-Khural-Khiid complex (Mongolia) [29]. As evidenced by the cited publications, melilite solid solutions growing from the cooling melt become progressively enriched in Na and Fe but depleted in Al and/or Mg [3, 17, 23].

In addition to the limitations of microanalytical facilities, the concentrations of trace elements in melilite can be hard to measure because they are low, especially in melilite coexisting with perovskite, apatite, titanite, loparite, etc., while the crystals are too small and contain abundant inclusions. Correspondingly, the scanty geochemical data are insufficient to highlight the fractionation trends in Ca-rich alkaline melts. The partition coefficients (K_d) of trace elements between melt and melilite solid solutions remain poorly constrained as well [5, 17, 30].

This study focuses on the chemical evolution of melilite solid solutions during crystallization of high-temperature Si-undersaturated combustion metamorphic (CM) melts rich in Ca and K, for the case of the Hatrurim Formation paralavas. The kalsilite-rankinite-wollastonite paralavas crystallized from the CM melts bear coarse crystals, including zoned melilites. The chosen natural CM system of the Hatrurim Formation is advantageous as the duration of crystallization far exceeded that in experimental systems and was long enough to equilibrate the mineral assemblages.

Methods

Two selected fresh paralava samples h-07-Gr-1 and h-07-51-3 were analyzed by several methods at the Analytical Center for Multielement and Isotope Research of the V.S.Sobolev Institute of Geology and Mineralogy (IGM, Novosibirsk, Russia). Electron probe microanalysis (EPMA) and laser ablation inductively coupled plasma mass spectrometry (LA-ICP-MS) were applied to characterize the compositions of seven coexisting minerals. The average element contents in bulk rock and separate minerals were then used to calculate the respective partition coefficients as a ratio of element concentrations in minerals to those in rocks: $K_d = [El_{mineral}]/[El_{rock}]$.

Scanning electron microscopy was used to identify the mineral species and study the morphology of crystals and mineral chemistry. The measurements were performed on a Tescan MIRA 3 MLU scanning electron microscope equipped with an AZtec Energy XMax-50+ microana-lysis system (Oxford Instruments NanoAnalysis Ltd.). The operating conditions were: 20 kV accelerating voltage, 1 nA beam current, 3 to 10 μm beam diameter, and 20 s count time. The mineral chemistry of melilite

and garnet was additionally analyzed on a Jeol JXA-8230 electron probe microanalyzer at an accelerating voltage of 20 keV, a beam current of 20 nA, a count time of 10 s for each analytical line, and a probe diameter of 2 μm, at a chamber vacuum of ≤ 0.001 Pa. The data quality was checked against the reference materials of standard minerals and synthetic compounds: wollastonite for Ca, garnet O-145 for Si, Al, Fe, Mg, garnet IGEM for Mn, orthoclase O-359-1 for K, albite for Na, and glass Gl-10 for Sr, as well as $BaTiSi_3O_9$ for Ba and Ti, $NiFe_2O_4$ for Ni, Cu_2O for Cu, and $ZnFe_2O_4$ for Zn. The detection limits (3σ criterion) were 0.01 wt.% for K_2O, 0.02 wt.% for CaO, MnO, and TiO_2, 0.03 wt.% for FeO, 0.04 wt.% for Al_2O_3, NiO, and CuO, 0.05 wt.% for SrO and ZnO, 0.06 wt.% for Na_2O, SiO_2, and BaO, and 0.10 wt.% for MgO.

Trace element abundances were determined by LA-ICP-MS on a Thermo Scientific iCAP Qc quadrupole inductively coupled plasma mass spectrometer with an Elemental Scientific NewWaveResearch 213 laser ablation platform (Nd:YAG laser, 213 nm wavelength, 10 Hz frequency, ~5 J/cm^2 fluence, and 50 μm beam diameter). The quality of determination was checked against the reference materials of NIST 612 glass standard and in-house standards of CaO concentrations (in apatite, rankinite, wollastonite, cuspidine, melilite, and garnet) and SiO_2 (in kalsilite). The instrument drift was monitored using the NIST 610 glass standard as an unknown sample. The duration of analysis was 90 s at each ablation spot, including 30 s for background measurements. The analyses were applied to flat polished sections and mineral grains extracted from monofractions. Trace elements were measured in 10-20 mg aliquots following the common method. The mineral names are abbreviated according to [31]: Aak – alumoakermanite ($NaCaAlSi_2O_7$), Ak – akermanite ($Ca_2MgSi_2O_7$), Ap – apatite, Brt – barite, Csp – cuspidine, CSH – Ca hydrosilicates, Fe^{2+}-Ak – ferroakermanite ($Ca_2Fe^{2+}Si_2O_7$), Fe^{3+}-Gh – ferrigehlenite ($Ca_2Fe^{3+}{}_2SiO_7$), Gh – gehlenite ($Ca_2Al_2SiO_7$), Grt – garnet, Hdy – hardystonite ($Ca_2ZnSi_2O_7$), Kls – kalsilite, Mag – magnetite, Mll – melilite, Rnk – rankinite, and Wo – wollastonite.

Garnet-melilite-wollastonite paralava from CM complexes of the Hatrurim Formation

The Hatrurim Basin (Israel) is the largest complex of CM rocks in the western side of the Dead Sea. Combustion metamorphism in the area involved the Maastrichtian Gareb Formation bioproductive marly limestone of the shelf facies during tectonic reactivation in the zone of the Dead Sea transform between 7 and 0.5 Ma. The Hatrurim Formation CM complex comprises garnet paralava (granitite), which is an exceptional group of Ca-rich melt rocks, along with high-temperature marbles and hornfels [24, 32, 33].

Veins of coarse paralava rich in Ti-garnet and melilite are occasionally found among high-temperature hornfels in the southwestern flank of the Gurim anticline within the Hatrurim Basin. The veins are commonly 1-3 cm thick, rarely reaching 5-10 cm (sample h-07-51-3). They are exposed on the surface and penetrate no more than 2-3 cm deep into fine-grained hornfels. The hornfels-paralava contacts are sharp and are delineated by quench zones that record rapid cooling of the CM melts.

The samples we studied represent Si-undersaturated Ca-rich rocks containing comparable moderate amounts of Fe_2O_3 and Al_2O_3, with K enrichment over Na. They have relatively high contents of phosphorus and fluorine due to the presence of phosphorite in the sedimentary protolith. The paralava samples selected for analyses (Fig.1, *a*, *b*) are compositionally similar though coming from the central parts of different veins, wt.%: 33.95-35.18 – SiO_2, 1.41-1.66 – TiO_2, 7.63-8.26 – Al_2O_3, 7.61-8.82 – Fe_2O_3, 0.54-0.60 – MgO, 40.76-41.41 – CaO, 0.35-0.40 – Na_2O, 0.41-1.12 – K_2O, 1.78-1.81 – P_2O_5, 0.09-0.18 – SO_3, and 0.42-0.48 – F. The samples differ slightly in the degree of secondary carbonation (0.89-1.42 wt.% CO_2) and hydration (1.54-3.08 wt.% H_2O), as well as in the percentages of retrograde minerals (CSH, zeolites, gypsum, thaumasite, and calcite).

The sedimentary protolith of the Hatrurim Formation paralavas was originally depleted in Mg, Mn, Rb, and Pb but enriched in such elements as P, S, Fe, V, Cr, Ni, Zn, Cu, Mo, Cd, and U, which are typical of bioproductive carbonate sediments deposited in anoxic marine environments [33]. The paralavas derived from this protolith bear the respective geochemical fingerprints (Table 1), with high contents

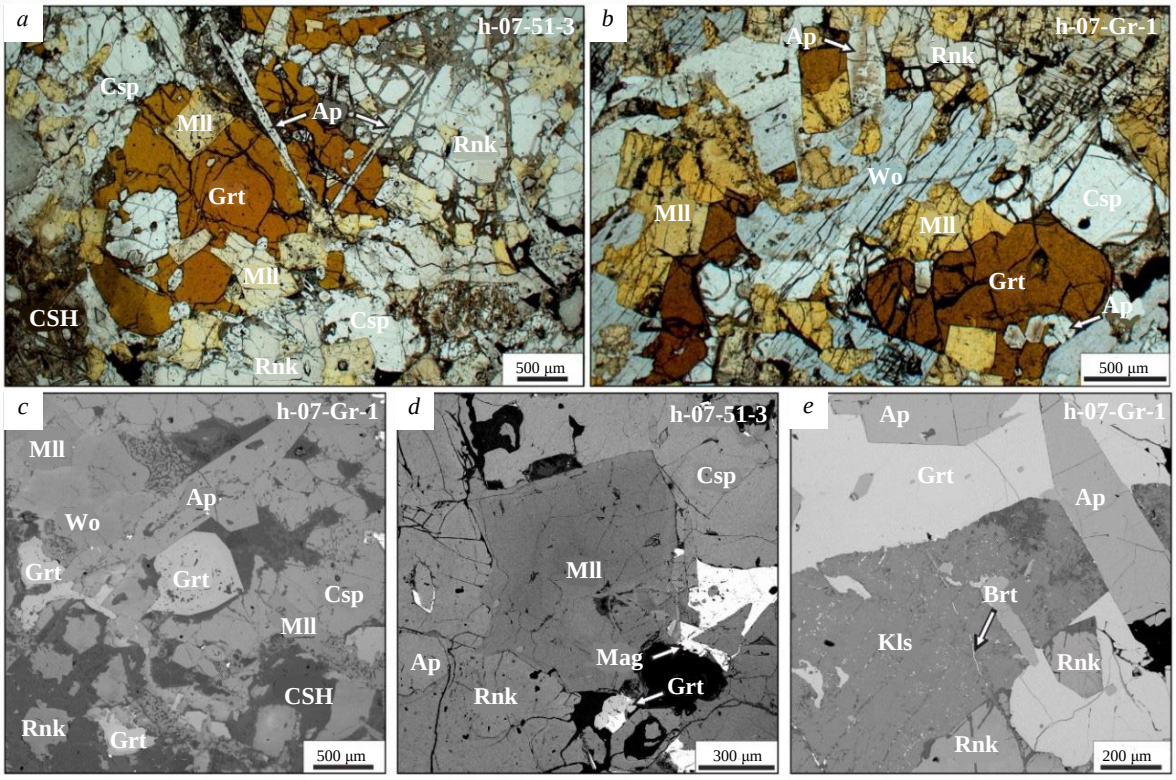

Fig.1. Morphology and spatial relations of rock-forming and accessory minerals in Hatrurim Formation high-Ca paralavas: *a-c* – general view of garnet paralava samples with anhedral wollastonites, rankinites, and cuspidines occupying up to 2/3 of the rock volume, as well as large poikilitic crystals of fluorapatite, grains and crystals of Ti-garnet and melilite; *d* – large zoned melilite crystal coexisting with rankinite, cuspidine, garnet, and fluorapatite; *e* – large anhedral grain of kalsilite with ingrown barite. Panels *a* and *b* are optical photographs; *c-e* are BSE images

of V, Cr, Ni, Cu, and Zn (hundreds of ppm), as well as Mo and U (tens of ppm). Furthermore, the high concentrations of Sr (1500 to 2400 ppm) and Ba (400 to 3200 ppm) in the paralavas likewise record the features of parent carbonate sediments that bear authigenic barite. According to an earlier detailed description [34], the representative paralava samples share similarity in trace-element chemistry.

Table 1

Average trace-element compositions of Ca-rich combustion metamorphic rocks, Hatrurim Formation (LA-ICP-MS data), ppm

Element	Sample							
	h-07-51-3				h-07-Gr-1			
	Mean, *n* = 5	*SD*	Min	Max	Mean, *n* = 5	*SD*	Min	Max
Sc	31.5	1.16	30.2	32.9	32.6	1.35	31.0	34.7
V	281	17.6	264	305	493	25.9	459	531
Cr	628	61.5	580	697	454	84.0	309	528
Mn	142	6.38	136	151	243	27.4	214	286
Co	13.9	0.51	13.1	14.5	22.0	1.05	20.7	23.3
Ni	504	37.9	452	539	802	53.5	726	868
Cu	297	46.7	241	360	705	265	487	1133
Zn	1369	108	1247	1544	2763	205	2613	3116
Ga	10.3	0.69	9.30	11.0	27.6	1.21	26.5	29.6
Rb	12.3	1.45	9.94	13.9	52.8	2.67	49.4	55.3
Sr	1655	118	1515	1802	2766	88.2	2639	2868

End of Table 1

Element	Sample							
	h-07-51-3				h-07-Gr-1			
	Mean, *n* = 5	*SD*	Min	Max	Mean, *n* = 5	*SD*	Min	Max
Y	72.2	3.87	67.7	76.7	90.3	3.38	87.4	95.2
Zr	200	11.3	185	213	272	16.3	250	292
Nb	20.9	0.83	19.9	21.9	42.0	2.27	38.8	45.1
Cd	7.59	2.57	5.13	10.3	25.3	10.4	13.0	40.1
Cs	0.11	0.02	0.09	0.15	0.42	0.05	0.38	0.50
Ba	466	14.0	451	483	3640	189	3435	3934
La	36.1	1.49	33.7	37.7	60.0	3.40	57.4	65.7
Ce	51.3	2.21	48.1	54.1	78.3	5.38	72.4	84.0
Pr	6.88	0.25	6.48	7.11	11.1	0.39	10.5	11.5
Nd	28.0	1.67	25.3	29.4	38.4	1.55	37.0	41.0
Sm	5.46	0.73	4.89	6.38	7.60	0.46	7.05	8.12
Eu	1.51	0.15	1.37	1.75	2.00	0.12	1.89	2.20
Gd	6.68	0.44	6.04	7.26	8.67	0.33	8.24	9.00
Tb	1.09	0.09	1.00	1.23	1.43	0.05	1.37	1.51
Dy	7.00	0.27	6.64	7.26	8.88	0.26	8.47	9.07
Ho	1.60	0.06	1.52	1.68	2.06	0.12	1.92	2.22
Er	5.11	0.17	4.95	5.35	6.42	0.32	6.06	6.79
Tm	0.73	0.04	0.68	0.78	0.85	0.05	0.78	0.92
Yb	5.32	0.37	5.00	5.95	6.07	0.29	5.72	6.42
Lu	0.79	0.04	0.72	0.82	0.95	0.07	0.87	1.06
Hf	5.45	0.20	5.14	5.64	6.29	0.21	5.96	6.51
Ta	1.40	0.09	1.33	1.56	2.37	0.10	2.22	2.49
Pb	8.55	0.32	8.05	8.92	24.0	1.49	22.3	25.7
Th	6.24	0.33	5.78	6.70	9.45	0.53	8.88	10.2
U	65.3	4.85	58.4	71.8	119	7.05	113	131

Note. n – number of analyses; *SD* – standard deviation; Min – minimum value; Max – maximum value.

The mineralogy of garnet paralava consists of wollastonite, rankinite, melilite solid solutions, Ti-andradite, fluorapatite, kalsilite, cuspidine (±flamite), and accessory carriers of Ba, V, Fe, Ni, and Cu. The crystallization sequence began with fluorapatite enclosing micrometer grains of K-Fe-Ni-Cu sulfides, phases of the zadovite-aradite solid solution series $BaCa_6((SiO_4)(PO_4))(PO_4)_2F$-$BaCa_6((SiO_4)(VO_4))(VO_4)_2F$, gurimite $Ba_3(VO_4)_2$, and barite (Fig.1, *a*, *c*; Fig.2). The following crystallized phases were Ca silicates (wollastonite and rankinite) and Ca fluorosilicate (cuspidine). Fresh wollastonite occurs as ≤ 2 mm subhedral

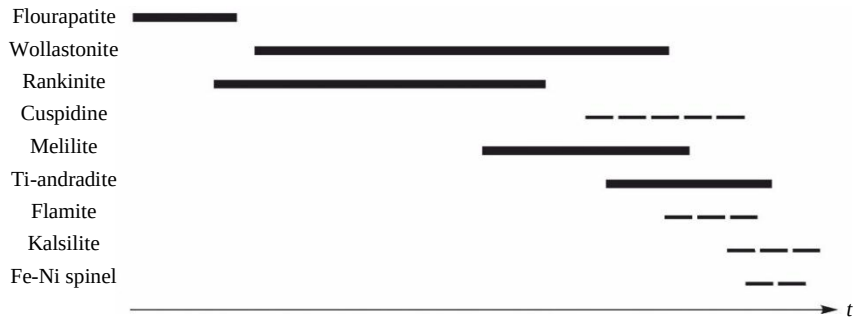

Fig.2. Crystallization sequence of minerals in the analyzed Hatrurim Formation high-Ca paralava samples. The solid line is the established crystallization sequence, the dotted line is the proposed sequence

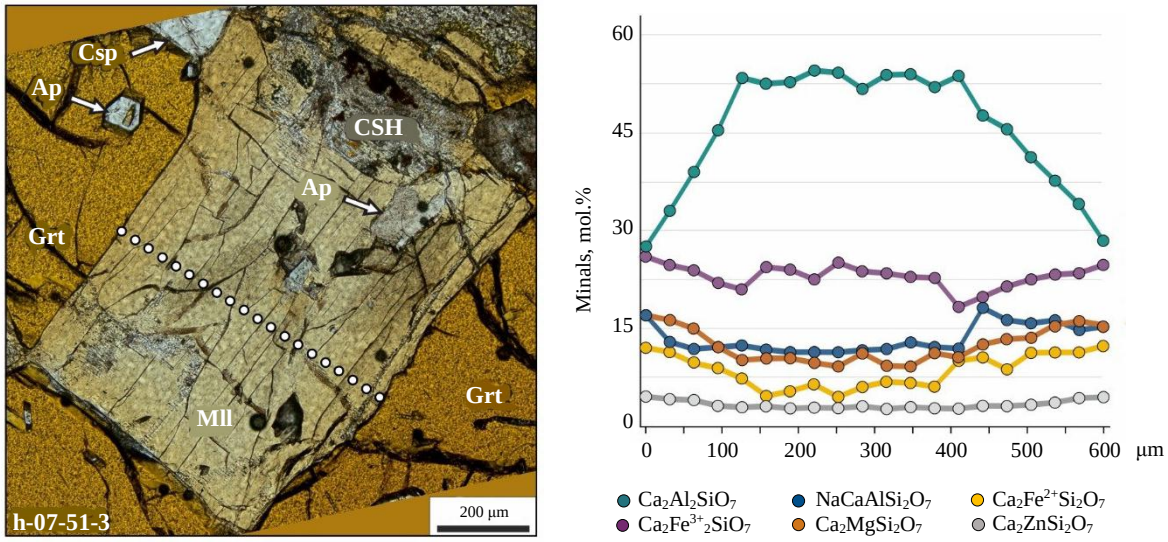

Fig.3. Profile of a zoned melilite crystal (endmembers in molar percentages) coexisting with garnet, cuspidine, and fluorapatite (optical photograph) from the Hatrurim Formation
High-Ca paralavas based on EPMA data

grains with fluorapatite inclusions (up to 0.2-0.4 mm). Rankinite forms anhedral grains (also ≤ 2 mm), often cracked and partly replaced by CSH (see Fig.1, *a-c*). The rankinite grains are mostly free from mineral inclusions (except for fluorapatite) but abound in melt inclusions. Cuspidine is found as anhedral grains (≤ 1 mm) or grain clusters (0.3-0.4 mm) and bears numerous fluorapatite inclusions (see Fig.1, *a-d*).

Melilite, which crystallized after or partly concurrently with Ca silicates, occurs as ≤ 1-2 mm zoned crystals or grains with sporadic inclusions of earlier fluorapatite and flamite (see Fig.1, *a, b, d*; Fig.3). The mineral is relatively stable against replacement, which makes it suitable for LA-ICP-MS analysis of trace elements and crystal zonation. Ti-andradite, a late phase in the crystallization sequence, not prone to replacement, exists as coarse zoned or sectorial crystals with inclusions of fluorapatite, wollastonite, Al-rich melilite, and ingrown flamite (see Fig.1, *a-c*). Kalsilite, crystallized the latest from CM melts, forms ≤ 1-2 mm anhedral grains, often fills the interstitial space, and contains multiple microinclusions, mostly barite; in some cases, the mineral is partly altered (see Fig.1, *e*). Fe-Ni spinel microcrysts is present sporadically. The lack of interstitial glass, along with the scarcity of melt inclusions in melilite, indicates that the rapidly cooling CaO-rich Si-undersaturated low-viscosity CM melts crystallized completely, like slags. The crystallization trends in the temperature range between 1500 and 1100 °C were reconstructed with reference to thermobarometry of melt inclusions, the $CaO–SiO_2–Al_2O_3$ phase diagram, and evidence from melting experiments [32].

Results

Major- and trace-element chemistry of minerals in paralavas. Fluorapatite contains on average, wt.%: 5.0 SiO_2, 3.9 SO_3, ≤ 1.4 SrO, ≤ 0.7 V_2O_3, and occasionally ≤ 1.1 FeO. Its average formula is $(Ca_{4.9}Sr_{\leq 0.1})_{\sum 5.0}(P_{2.4}Si_{0.4}S_{0.2}V_{\leq 0.1})_{\sum 3.0}O_{12.0}F_{0.9}(OH)_{0.1}$ (n = 21). The mineral bears 400-900 ppm of total REE, including 390-770 ppm ΣLREE, at ≤ 85.0 ppm Th and 144 ppm U. Fluorapatite from sample h-07-51-3 also contains 24.6 ppm of Pb on average (Tables 2, 3, Supplements 1, 2).

Wollastonite has an average composition of $Ca_{1.0}Si_{1.0}O_{3.0}$ (n = 22), with minor amounts of FeO (≤ 0.5 wt.%) and TiO_2 (≤ 0.4 wt.%) in a few grains. Trace elements have quite low uniform contents, with common Sr (650-1200 ppm). The concentrations of Ba are an order of magnitude lower (9.00 to 90.0 ppm). The REE total is 30.0-80.0 ppm; ≤ 800 ppm Ti (Table 3, Supplement 1).

Table 2

Average contents of REE and Y in rock-forming and minor minerals from Ca-rich combustion metamorphic rocks, Hatrurim Formation (LA-ICP-MS data), ppm

Element	Y	La	Ce	Pr	Nd	Sm	Eu	Gd	Tb	Dy	Ho	Er	Tm	Yb	Lu
Fluorapatite, h-07-51-3 (n = 3)															
Mean	65.4	207	277	27.6	80.0	12.0	2.85	12.4	1.44	7.88	1.60	4.84	0.59	3.46	0.46
SD	12.3	46.6	101	3.35	3.48	2.09	0.93	4.32	0.55	2.69	0.54	2.48	0.32	2.09	0.25
Min	57.2	163	214	24.7	76.1	10.4	2.28	9.44	1.06	6.19	1.21	3.12	0.39	2.25	0.32
Max	79.6	255	394	31.3	82.8	14.3	3.93	17.3	2.07	11.0	2.21	7.68	0.96	5.87	0.75
K_d	0.91	5.74	5.14	4.00	2.86	2.19	1.88	1.85	1.31	1.12	1.00	0.95	0.81	0.65	0.59
Wollastonite, h-07-51-3 (n = 4)															
Mean	21.3	16.6	20.6	3.97	14.5	3.35	1.17	3.84	0.78	3.15	0.96	1.91	0.48	1.43	0.47
SD	12.9	6.07	12.6	2.02	7.33	2.39	1.20	2.91	0.85	2.49	1.00	1.51	0.68	1.30	0.71
Min	4.26	10.9	9.66	1.85	5.56	0.91	0.20	0.55	0.10	0.48	0.10	0.29	0.05	0.24	0.06
Max	31.4	24.9	38.5	6.67	22.8	6.47	2.90	7.46	2.02	6.28	2.39	3.76	1.50	3.12	1.53
K_d	0.30	0.46	0.40	0.58	0.52	0.61	0.77	0.58	0.72	0.45	0.60	0.37	0.66	0.27	0.60
Rankinite, h-07-51-3 (n = 3)															
Mean	36.6	20.0	20.8	4.14	14.7	2.69	0.74	3.51	0.54	3.52	0.80	2.32	0.33	2.01	0.33
SD	11.1	15.4	21.3	2.12	6.75	0.40	0.03	0.35	0.14	1.17	0.26	0.72	0.09	0.38	0.08
Min	23.9	10.4	812	2.85	9.43	2.25	0.71	3.17	0.38	2.21	0.49	1.49	0.22	1.59	0.24
Max	44.3	37.7	45.4	6.59	22.3	3.02	0.77	3.88	0.63	4.43	0.97	2.76	0.39	2.32	0.40
K_d	0.51	0.55	0.41	0.60	0.53	0.49	0.49	0.52	0.50	0.50	0.50	0.45	0.45	0.38	0.42
Cuspidine, h-07-Gr-1 (n = 10)															
Mean	100	28.0	97.7	6.90	26.4	6.13	1.67	7.59	1.35	9.74	2.57	8.70	1.36	10.7	1.65
SD	18.5	5.99	10.5	0.82	2.58	0.75	0.25	1.18	0.22	1.54	0.48	1.71	0.26	2.65	0.31
Min	75.5	20.8	79.1	5.67	24.3	5.31	1.29	5.89	0.96	7.34	1.85	6.08	1.01	7.48	1.28
Max	139	39.8	111	8.12	32.0	7.69	2.18	9.67	1.76	13.1	3.49	11.7	1.96	16.8	2.42
K_d	1.11	0.47	1.25	0.62	0.69	0.81	0.84	0.88	0.94	1.10	1.25	1.35	1.59	1.76	1.73
Garnet – low-Ti cores, h-07-51-3 (n = 2)															
Mean	103	20.1	76.0	12.5	55.8	12.7	3.44	13.0	1.88	12.0	2.48	8.32	1.21	8.79	1.51
SD	8.01	4.00	2.52	2.21	7.46	1.80	0.21	1.11	0.15	0.22	0.32	0.78	0.01	0.40	0.09
Min	97.2	17.3	74.3	10.9	50.5	11.4	3.29	12.2	1.77	11.8	2.26	7.76	1.20	8.50	1.45
Max	109	23.0	77.8	14.0	61.0	13.9	3.59	13.8	1.99	12.1	2.71	8.87	1.22	9.07	1.58
K_d	1.42	0.56	1.48	1.81	1.99	2.32	2.27	1.94	1.72	1.71	1.55	1.63	1.66	1.65	1.93
Garnet – high-Ti rims, h-07-51-3 (n = 6)															
Mean	401	13.0	79.5	9.54	59.3	19.9	6.32	31.2	5.34	40.0	9.65	32.2	4.81	36.0	5.98
SD	88.5	3.87	28.0	2.71	14.3	4.57	1.40	6.36	1.36	10.1	2.73	9.27	1.36	10.1	1.48
Min	326	8.50	43.0	5.96	42.2	14.2	4.51	25.7	3.97	32.0	7.88	26.6	3.79	29.2	4.69
Max	573	17.2	112	12.6	76.8	24.4	8.22	42.3	7.81	59.2	15.0	50.5	7.43	56.0	8.77
K_d	5.55	0.36	1.55	1.39	2.12	3.65	4.17	4.66	4.88	5.72	6.03	6.30	6.62	6.78	7.61
Melilite – low-Fe cores, h-07-51-3 (n = 5)															
Mean	1.53	1.85	1.94	0.41	1.59	0.31	0.09	0.32	0.04	0.21	0.04	0.11	0.01	0.07	0.01
SD	0.16	0.10	0.16	0.03	0.18	0.06	0.01	0.04	0.01	0.03	0.00	0.03	0.00	0.02	0.00
Min	1.32	1.71	1.76	0.37	1.39	0.23	0.08	0.25	0.03	0.17	0.03	0.08	0.01	0.04	0.01
Max	1.71	1.95	2.18	0.44	1.83	0.37	0.09	0.36	0.05	0.25	0.04	0.14	0.02	0.10	0.01
K_d	0.02	0.05	0.04	0.06	0.06	0.06	0.06	0.05	0.04	0.03	0.02	0.02	0.02	0.01	0.01
Melilite – high-Fe rims, h-07-51-3 (n = 11)															
Mean	0.67	4.67	4.86	0.74	2.44	0.28	0.09	0.23	0.02	0.11	0.02	0.05	0.01	0.04	0.01
SD	0.35	1.17	1.17	0.11	0.54	0.12	0.03	0.12	0.02	0.08	0.02	0.04	0.01	0.05	0.01
Min	0.10	3.05	2.78	0.58	1.43	0.11	0.04	0.05	0.00	0.01	0.00	0.01	0.00	0.00	0.00
Max	1.29	6.88	6.78	0.89	3.60	0.54	0.14	0.51	0.06	0.33	0.07	0.14	0.02	0.16	0.02
K_d	0.01	0.13	0.09	0.11	0.09	0.05	0.06	0.03	0.02	0.02	0.01	0.01	0.01	0.01	0.01
Kalsilite, h-07-Gr-1 (n = 21)															
Mean	1.55	3.97	5.57	0.59	1.80	0.31	0.12	0.25	0.04	0.21	0.04	0.14	0.02	0.15	0.03
SD	0.72	2.20	2.62	0.32	0.87	0.15	0.07	0.12	0.02	0.09	0.02	0.08	0.01	0.06	0.04
Min	0.66	1.43	2.25	0.21	0.61	0.12	0.03	0.08	0.01	0.07	0.01	0.05	0.00	0.06	0.00
Max	2.94	9.18	9.86	1.15	3.30	0.60	0.27	0.51	0.08	0.37	0.09	0.32	0.05	0.25	0.19
K_d	0.02	0.07	0.07	0.05	0.05	0.04	0.06	0.03	0.03	0.02	0.02	0.02	0.03	0.02	0.03

Table 3

Average trace-element compositions of rock-forming and minor minerals from Ca-rich combustion metamorphic rocks, Hatrurim Formation (LA-ICP-MS data), ppm

Element	Sc	Ti	V	Cr	Mn	Co	Ni	Cu	Zn	Ga	Rb	Sr	Zr	Nb	Ba	Hf	Ta	Th	U
Flourapatite, h-07-51-3 (n = 3)																			
Mean	2.38	578	1662	61.3	137	8.82	103	572	723	7.39	4.60	3296	10.9	1.39	1128	0.15	0.02	25.1	37.8
SD	0.35	370	1129	76.1	153	14.0	114	204	1035	4.38	5.72	1427	8.87	1.14	873	0.15	0.004	3.46	14.5
Min	1.99	215	531	13.9	19.1	0.55	6.11	427	69.9	2.76	0.56	1665	5.20	0.59	127	0.05	0.02	22.3	21.1
Max	2.67	954	2788	149	310	25.0	229	716	1916	11.5	8.65	4312	21.1	2.70	1729	0.32	0.03	29.0	47.2
K_d	0.08	0.07	5.91	0.10	0.96	0.63	0.20	1.92	0.53	0.72	0.38	1.99	0.05	0.31	2.42	0.03	0.02	4.03	0.58
Wollastonite, h-07-51-3 (n = 4)																			
Mean	7.24	485	19.3	3.41	26.1	0.94	7.38	0.25	7.02	0.49	0.75	836	2.43	0.36	12.6	0.28	0.37	0.67	0.37
SD	0.88	152	6.79	0.48	11.8	0.56	1.70	0.001	3.36	0.23	0.18	147	3.28	0.64	4.57	0.51	0.51	0.76	0.11
Min	6.05	247	13.0	3.07	17.7	0.57	6.18	0.25	4.65	0.32	0.63	662	0.17	0.01	9.00	0.01	0.01	0.14	0.24
Max	8.10	680	26.5	3.75	34.4	1.58	8.58	0.25	9.40	0.65	0.88	1011	7.13	1.31	17.7	1.05	0.73	1.54	0.46
K_d	0.23	0.06	0.07	0.01	0.18	0.07	0.01	0.01	0.01	0.05	0.06	0.50	0.01	0.02	0.03	0.05	0.26	0.11	0.01
Rankinite, h-07-51-3 (n = 3)																			
Mean	6.00	139	16.8	11.7	25.5	0.91	4.78	100	35.9	0.21	bdl	793	0.14	0.02	10.0	bdl	bdl	0.12	0.07
SD	0.34	10.4	13.5	10.3	1.25	0.28	0.12	88.8	5.72	0.12	–	7.48	0.07	0.01	1.03	–	–	0.09	0.04
Min	5.73	130	8.85	0.09	24.7	0.62	4.70	1.24	29.6	0.12	bdl	787	0.07	0.01	9.31	bdl	bdl	0.07	0.03
Max	6.39	150	32.4	19.8	26.4	1.18	4.87	173	40.7	0.34	bdl	798	0.20	0.03	10.8	bdl	bdl	0.22	0.11
K_d	0.19	0.02	0.06	0.02	0.18	0.07	0.01	0.34	0.03	0.02	–	0.48	0.01	0.01	0.02	–	–	0.02	0.01
Cuspidine, h-07-Gr-1 (n = 10)																			
Mean	15.8	909	31.4	21.2	33.4	0.37	1.79	3.25	6.70	0.59	1.82	1434	1112	164	53.4	21.5	9.90	24.3	1347
SD	2.40	160	12.3	19.2	6.14	0.12	0.99	2.60	3.74	0.35	1.51	264	262	32.2	30.0	5.52	3.20	4.63	492
Min	12.8	702	17.1	7.61	26.2	0.19	0.85	0.12	1.75	0.16	0.14	984	637	86.9	23.1	12.9	2.42	17.4	547
Max	21.7	1257	54.9	34.7	42.4	0.61	3.38	8.47	10.8	1.38	4.30	1971	1590	197	95.0	34.0	14.0	33.1	2059
K_d	0.48	0.07	0.06	0.05	0.14	0.02	0.01	0.01	0.01	0.02	0.03	0.52	4.08	3.92	0.01	3.41	4.18	2.57	11.35
Garnet – low-Ti cores, h-07-51-3 (n = 2)																			
Mean	27.1	28498	882	29.3	37.6	1.93	71.2	1.31	20.9	5.39	0.82	51.4	231	80.4	0.28	3.98	6.97	20.8	113
SD	3.09	6576	6.56	5.14	11.8	0.62	16.1	0.09	3.00	0.78	0.01	4.65	22.7	6.08	0.17	0.37	0.77	3.44	17.6
Min	24.9	23848	817	25.7	29.3	1.49	59.8	1.25	18.8	4.84	0.81	48.1	215	76.1	0.15	3.72	6.42	18.4	101
Max	29.3	33148	827	32.9	45.9	2.37	82.6	1.38	23.0	5.94	0.83	54.7	247	84.8	0.40	4.24	7.51	23.3	126
K_d	0.86	3.38	2.92	0.05	0.26	0.14	0.14	0.01	0.02	0.52	0.07	0.03	1.16	3.85	0.01	0.73	4.98	3.34	1.73
Garnet – high-Ti rims, h-07-51-3 (n = 6)																			
Mean	202	63013	245	4581	48.9	1.37	82.8	306	213	5.60	bdl	35.7	2190	38.4	0.30	51.9	7.29	16.6	24.1
SD	66.3	9036	95.4	3536	14.2	0.40	23.7	648	366	1.15	–	8.94	516	11.9	0.33	15.6	1.45	5.41	7.86
Min	159	54631	141	1584	31.5	0.85	50.8	4.22	37.8	3.91	bdl	23.9	1669	24.3	0.03	38.5	5.73	11.8	16.6
Max	336	79402	339	10609	61.6	1.86	104	1621	959	6.97	bdl	43.7	2873	51.2	0.73	82.0	9.67	24.0	33.6
K_d	6.43	7.47	0.87	7.30	0.34	0.10	0.16	1.03	0.16	0.54	–	0.02	10.95	1.84	0.01	9.51	5.21	2.65	0.37
Melilite – low-Fe cores, h-07-51-3 (n = 5)																			
Mean	4.38	122	1.35	5.21	30.2	20.0	297	281	1655	25.5	2.40	1387	1.29	0.03	26.3	bdl	bdl	0.02	0.02
SD	0.52	11.0	0.83	1.12	4.47	2.90	29.8	327	121	1.27	1.89	245	2.72	0.03	8.56	–	–	0.02	0.02
Min	3.46	109	0.52	4.09	23.4	16.9	227	92.5	1475	24.3	0.79	1014	0.07	0.01	17.3	bdl	bdl	0.01	0.01
Max	4.72	133	2.53	6.39	35.8	22.8	301	857	1798	27.5	4.97	1636	6.16	0.09	36.4	bdl	bdl	0.05	0.05
K_d	0.14	0.01	0.01	0.01	0.21	1.43	0.55	0.94	1.21	2.47	0.20	0.84	0.01	0.01	0.06	–	–	0.01	0.01
Melilite – high-Fe rims, h-07-51-3 (n = 11)																			
Mean	5.65	184	18.0	10.9	283	46.6	790	515	7547	25.8	0.73	4021	0.11	0.07	806	bdl	bdl	0.07	0.23
SD	0.49	30.3	22.3	13.4	199	13.7	219	377	1980	2.38	0.56	1809	0.13	0.12	996	–	–	0.09	0.10
Min	4.97	130	0.60	1.85	54.2	31.3	459	76.3	2574	21.2	0.01	2047	0.01	0.01	39.7	bdl	bdl	0.01	0.11
Max	6.49	231	59.3	45.3	729	69.3	1154	1136	10355	29.7	1.73	6469	0.48	0.38	3019	bdl	bdl	0.28	0.37
K_d	0.18	0.02	0.06	0.02	1.99	3.34	1.57	1.73	5.51	2.50	0.06	2.43	0.01	0.01	1.73	–	–	0.01	0.01
Kalsilite, h-07-Gr-1 (n = 21)																			
Mean	9.17	216	51.1	55.4	27.5	0.56	2.82	62.6	68.7	14.8	348	317	55.8	8.72	2032	1.26	0.26	0.56	1.87
SD	3.88	96.5	86.5	75.6	12.1	0.38	2.65	73.4	77.0	12.0	314	149	25.1	3.65	2528	0.61	0.12	0.25	1.04
Min	4.22	86.2	2.47	2.46	11.2	0.11	0.68	2.30	1.71	3.19	33.9	103	25.0	4.04	273	0.52	0.10	0.25	0.46
Max	14.7	347	389	281	48.9	1.67	13.5	230	310	42.5	1351	806	96.2	14.9	8563	2.36	0.43	0.98	4.12
K_d	0.28	0.02	0.10	0.12	0.11	0.03	0.01	0.09	0.02	0.53	6.59	0.11	0.20	0.21	0.56	0.20	0.11	0.06	0.02

Notes: bdl – below detection limit; flourapatite contains 2.31 ppm Cd (K_d = 0.31) and 24.6 ppm Pb (K_d = 2.87); high-Ti garnet rims contain 1.75 ppm Cd (K_d = 0.23); high-Fe melilite rims contain 1.97 ppm Cd (K_d = 0.26); kalsilite contains 2.68 ppm Cs (K_d = 6.32) and 8.45 ppm Pb (K_d = 0.35); cuspidine contains 1.59 ppm Pb (K_d = 0.07).

Rankinite having an average composition of $Ca_{3.0}Si_{2.0}O_{7.0}$ (n = 17) contains only FeO (≤ 0.7 wt.%) and Sr (750-1300 ppm) impurities. The total content of REE is 40.0 to 130 ppm; Ti is ≤ 250 ppm (see Table 3, Supplement 1).

The composition of cuspidine fits the theoretical formula $Ca_{4.0}Si_{2.0}O_{7.0}F_{2.0}$ (n = 12). It stores a moderate amount of Sr (950-2000 ppm), low Ba (23.0-95.0 ppm), high concentrations of high-field strength elements, HFSE (700-1300 ppm Ti, 630-1600 ppm Zr, and 86.0-200 ppm Nb), and up to 2100 ppm U; ΣREE is quite low (≤ 260 ppm), with ≤ 35.0 ppm Th, ≤ 34.0 ppm Hf, and ≤ 14.0 ppm Ta (Tables 2, 3, Supplements 1, 2).

Melilites changed considerably its major-element chemistry while growing (Fig.3, 4), which is evident in the profile of a zoned crystal and tabulated data (Table 4, Supplement 3). The composition of melilite in two paralava samples was determined in 80 analyses of core and 65 analyses of rim zones. The trend is from relatively high Al_2O_3 (23.7 wt.% on average) and moderate contents of FeO (6.7 wt.%) and MgO (1.9 wt.%) at low Na_2O (0.7 wt.%) and K_2O (0.4 wt.%) in the core to lower Al_2O_3 (10.8 wt.%) but higher FeO (8.9 wt.%) and MgO (5.0 wt.%) in the rim. Sodium, which is minor in the rock (0.4 wt.% Na_2O), became a major element in melilite having reached an average of 1.9 wt.% at the final growth stage. Note that the amounts of potassium and zinc are minor in the rock (0.4-1.1 K_2O wt.% and 1250-3120 ppm Zn) but comparable in late melilite (0.8 wt.% K_2O and 1.2 wt.% ZnO on average).

Melilite in garnet paralava is the principal carrier of Zn (up to 7000 ppm in the core and 17,000 ppm in the rim), Co (up to 90.0 ppm), and Ga (up to 63.0 ppm) and shows Sr enrichment of 1000-7500 ppm. The contents of these elements are systematically higher in the rim, where the contents of Cu, Ni, and Mn are high as well: up to 4016 ppm Cu, 2060 ppm Ni, and 729 ppm Mn (see Table 3, Supplement 1).

The formulas corresponding to the average core and rim compositions of melilite crystals in the Hatrurim garnet paralava are, respectively, $Gh_{53}Fe^{3+}$-$Gh_{22}Ak_{15}Fe^{2+}$-$Ak_6Hdy_2Aak_2$ and Gh_2Fe^{3+}-$Gh_{34}Ak_{36}Fe^{2+}$-$Ak_1Hdy_6Aak_{21}$. The core is dominated by the gehlenite and ferrigehlenite endmembers ($Gh_{53}Fe^{3+}$-Gh_{22}), while the akermanite and ferroakermanite total is 21 mol.% ($Ak_{15}Fe^{2+}$-Ak_6); the contributions of the Na and Zn endmembers are modest (Hdy_2Aak_2). The amounts of the akermanite (Ak_{36}) and ferrigehlenite (Gh_2Fe^{3+}-Gh_{34}) endmembers in the rim are similar, while the molar percentages of the Na and Zn minals increase to 21 mol.% (Na-bearing alumoakermanite Aak_{21}) and 6 mol.% (Zn-bearing Hdy_6). The total of REE does not exceed 20 ppm.

Garnet, one of late phases, occurs as ≤ 2-3 mm zoned crystals with inclusions of fluorapatite, wollastonite, melilite, and ingrown flamite (see Fig.1, *a*-*c*). The core composition is similar to andradite,

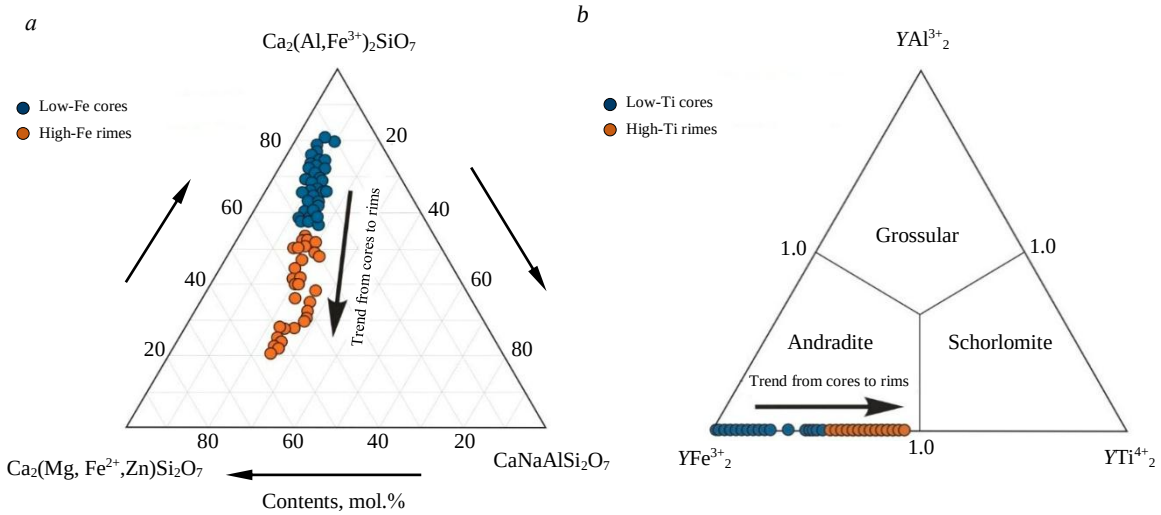

Fig.4. Melilite (*a*) and garnet (*b*) from the Hatrurim Formation high-Ca paralava in ternary diagrams:
a – melilite composition in the $Ca_2(Mg,Fe^{2+},Zn)Si_2O_7$–$Ca_2(Al,Fe^{3+})_2SiO_7$–$CaNaAlSi_2O_7$ diagram, mol.%;
b – garnet composition in the YFe^{3+}_2–YAl^{3+}_2–YTi^{4+}_2 diagram (formula based on 8 cations).
Plotted for *Y* occupancy proceeding from the general formula of garnet-group minerals $X_3Y_2Z_3O_{12}$, according to the nomenclature from [35]

with 5.3 wt.% TiO_2 and 820-3350 ppm V on average (n = 15), and corresponds to the formula $Ca_{3.0}(Fe^{3+}_{1.6}Ti_{0.3}V_{\leq 0.01})_{\sum 2.0}(Si_{2.6}Al_{0.2}Fe^{3+}_{0.2})_{\sum 3.0}O_{12.0}$. The rim is enriched in TiO_2 (11.3 wt.% on average) and contains 1000 to 10,000 ppm Cr, 150 to 2990 ppm Zr, 80.0 to 600 ppm Y, 15.0 to 340 ppm Sc, 24.0 to 125 ppm Nb, ≤ 82.0 ppm Hf, and ≤ 11.0 ppm Ta. The formula of the average rim composition is $Ca_{3.0}(Fe^{3+}_{1.2}Ti_{0.7}Cr_{0.04}Sc_{\leq 0.01}Fe^{2+}_{\leq 0.01})_{\sum 2.0}(Si_{2.2}Fe^{3+}_{0.5}Al_{0,3})_{\sum 3.0}O_{12.0}$ (n = 60) (Supplement 4). Garnets store Th (≤ 30.0 ppm) and U (≤ 130 ppm) at ΣREE reaching 570 ppm (see Tables 2, 3, Supplements 1, 2).

Table 4

Representative analyses of melilite from Ca-rich combustion metamorphic rocks, Hatrurim Formation (EPMA data), wt.%

Component	1	2	3	4	5	6	7	8	9	10	11	12
SiO_2	25.31	26.29	27.04	27.19	27.85	28.75	29.14	30.27	31.41	31.71	32.73	34.32
Al_2O_3	24.17	23.62	22.94	22.79	20.94	19.23	18.33	17.31	16.53	14.59	12.89	11.94
FeO*	0.00	0.00	0.00	0.15	0.00	0.53	0.86	0.45	0.00	0.00	0.33	0.00
Fe_2O_3*	7.29	7.73	7.40	7.93	7.82	7.95	8.68	9.94	8.35	9.29	10.31	10.07
MgO	1.84	2.06	2.16	1.86	2.27	2.54	2.62	2.77	3.05	3.10	3.63	3.88
CaO	39.49	39.23	39.44	38.07	38.41	37.89	37.48	37.55	37.16	36.23	36.55	36.21
Na_2O	0.40	0.47	0.49	0.80	0.63	0.77	1.02	0.92	1.23	1.67	1.54	1.71
K_2O	0.17	0.25	0.30	0.42	0.42	0.53	0.43	0.60	0.67	0.54	0.63	0.80
ZnO	0.46	0.70	0.41	0.49	0.68	0.83	0.92	1.13	0.85	1.47	1.61	1.02
Total	99.13	100.35	100.18	99.70	99.02	99.02	99.48	100.94	99.25	99.01	100.22	99.95
Coefficients calculated for 7 oxygen atoms												
Si^{4+}	1.227	1.267	1.311	1.325	1.193	1.317	1.438	1.543	1.314	1.384	1.502	1.505
Al^{3+}	1.301	1.267	1.214	1.170	1.343	1.167	0.951	0.757	1.141	1.024	0.815	0.788
Fe^{2+}	0.000	0.000	0.000	0.006	0.000	0.021	0.034	0.018	0.000	0.000	0.013	0.000
Fe^{3+}	0.257	0.271	0.260	0.283	0.278	0.283	0.310	0.358	0.299	0.331	0.367	0.363
Mg^{2+}	0.143	0.151	0.155	0.176	0.129	0.160	0.208	0.238	0.186	0.181	0.219	0.232
Ca^{2+}	1.963	1.981	1.939	1.946	1.995	1.946	1.892	1.825	1.955	1.903	1.839	1.888
Na^+	0.057	0.045	0.061	0.071	0.037	0.058	0.107	0.161	0.054	0.104	0.153	0.120
K^+	0.018	0.018	0.024	0.020	0.010	0.025	0.031	0.040	0.018	0.032	0.033	0.044
Zn^{2+}	0.019	0.014	0.020	0.027	0.016	0.024	0.030	0.039	0.032	0.041	0.051	0.051
Minals, mol.%												
$Ca_2Al_2SiO_7$	49.69	47.58	45.32	41.99	51.29	41.61	26.47	11.83	39.71	29.12	14.48	14.89
$Ca_2Fe^{3+}{}_2SiO_7$	26.88	28.20	27.08	29.15	28.99	29.12	31.93	37.57	30.76	34.44	37.95	38.25
$Ca_2MgSi_2O_7$	15.79	14.88	16.88	16.99	13.45	16.46	21.42	24.97	19.14	18.83	22.65	24.45
$NaCaAlSi_2O_7$	6.16	7.36	8.53	8.68	4.60	8.18	13.60	19.65	7.10	13.34	18.30	15.98
$Ca_2Fe^{2+}Si_2O_7$	0.00	0.00	0.00	0.62	0.00	2.16	3.50	1.89	0.00	0.00	1.34	0.00
$Ca_2ZnSi_2O_7$	1.46	1.98	2.19	2.57	1.67	2.47	3.09	4.09	3.29	4.27	5.27	6.43

* Contents of FeO and Fe_2O_3 were calculated based on the stoichiometric composition.

Kalsilite has an average composition of $(K_{0.9}Na_{0.1})_{\sum 1.0}(Al_{0.9}Fe_{0.1})_{\sum 1.0}Si_{1.0}O_{4.0}$ (n = 11) and commonly contains notable amounts of FeO (3.0-3.9 wt.%) and Na_2O (0.3-1.0 wt.%). The mineral is the main host of Ba (≤ 8500 ppm) and the only carrier of Rb (≤ 1350 ppm), while its Sr contents are moderate (100 to 800 ppm). The total of REE is as low as 5 to 26 ppm (see Table 3, Supplement 1).

Discussion

Crystallization sequence of minerals in paralavas and element partitioning trend. The crystallization scenario of Si-undersaturated CM melts, with originally high contents of Ca at moderate Fe and K, consisted in successive growth of silicates with a progressively decreasing Ca/Si ratio [32, 34]. The trend lacks peritectic reactions which typically appear in the phase diagrams describing the crystallization of alkaline Si-undersaturated magmas and obscure the patterns of element fractionation in the presence of melilite solid solutions [17, 36, 37]. This feature of the Hatrurim paralava allows estimating K_d of trace elements between melilite solid solutions and the coexisting silicates and fluorapatite.

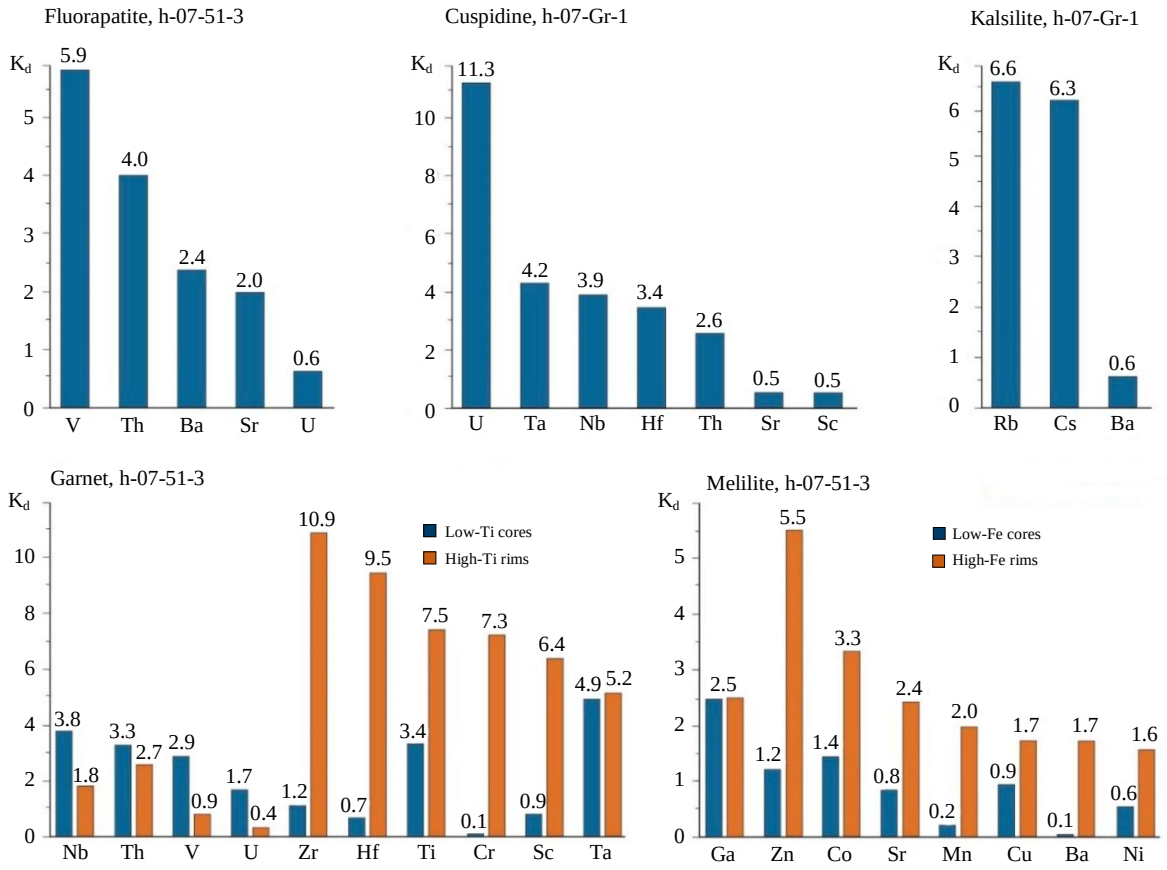

Fig.5. Partition coefficients of typical trace elements in rock-forming minerals from the Hatrurim Formation high-Ca paralavas

Fluorapatite begins the crystallization of CM melts and is the main storage of V (K_d = 2.7-5.9), LREE, MREE (K_d = 1.1-5.7), and Th (K_d = 4.0-5.2). It is always enriched in Sr (K_d = 1.3-2.0) and stores notable amounts of U (up to 144 ppm, at K_d = 0.4-0.6) (see Tables 2, 3, Supplements 1, 2; Fig.5, 6). The ubiquitous presence of SiO_2 and very low Na_2O contents (< 0.2 wt.%) provide evidence for the $Ca^{2+} + P^{5+} \rightarrow REE^{3+} + Si^{4+}$ isomorphic substitution.

The crystallization of fluorapatite is followed by Ca silicates (wollastonite and rankinite) which occupy up to 2/3 of the rock volume in total and have low contents of minor and trace elements. As a result, most of impurities in the residual melt increase dramatically. At this stage, only Ba, V, and LREE become partly immobilized in fluorapatite and in accessory Ba-V phases. Wollastonite and rankinite show notable enrichment only in Sr ($K_d \leq 0.5$) (see Table 3, Supplement 1). This crystallization scenario of CM melts influences greatly the major-element chemistry of melilite solid solutions and the trace-element composition of cuspidine. The final cooling stage also produces Ti-andradite rich in HFSE and REE and kalsilite as a major carrier of Rb.

The composition of melilite, which crystallized after Ca silicates, evolves from high Al contents at high temperatures to enrichment in Mg, Fe, Na, and Zn (see Fig.4), when the temperature decreases. Analysis of core and rim, which was possible in large zoned crystals, revealed distinct correlation between the partition coefficients of trace elements and the composition of melilite solid solutions (see Table 3, Supplement 1; Fig.5). Out of the four above-mentioned elements in the rim, only iron reached a major-element level in rock/melt (7.6-8.8 wt.% Fe_2O_3). The others, including Mg and Na, should be considered as impurities. Melilite solid solutions can accumulate chalcophile elements (Zn, Co, and Ni), as well as Ga, a geochemical equivalent of Al, at all growth stages. The respective partition coefficients increase as the composition of the growing mineral evolves from high Al toward higher Na, Fe^{3+}, Mg, and Zn contents. A notable amount of Cu is found in late melilite only. The

maximum Sr, Ba, and Mn concentrations are likewise common to the rim of melilite crystals with low gehlenite but high percentages of the alumoakermanite (Aak_{11-28}) and akermanite (+ferroakermanite) ($Ak+Fe^{2+}$-Ak_{21-42}) endmembers. The partition coefficients of Co, Zn, and Ni vary from 0.5 to 2.5 in the core and reach 5.5 in the rim (see Fig.5), whereas the content of Ga is proportional to the share of the gehlenite endmember. Zn and Ga enrichment ($K_d > 1$) was reported earlier for magmatic melilite as well. Therefore, these elements become incorporated into the structure of the host mineral by the (Mg, Fe^{2+}) → Zn^{2+} and $Al^{3+} \rightarrow Ga^{3+}$ substitutions. In general, the composition trend of CM melilite results from the uptake of Al in the early generation (crystal core) and respective enrichment of the residual melt in the major elements of Mg, Fe, and Na, minor iron-group elements (Co, Ni, Mn), and such elements as Zn and Cu, as well as Ga, Sr, Ba and Mn.

The structural affinity of melilite to chalcophile elements is known from directed synthesis technologies and is used in the production of the respective composite materials [7]. Meanwhile, melilite from the Hatrurim paralava owes its prominent enrichment in these elements not only to the protolith chemistry [33], but also to unusual oxidizing conditions during the crystallization of CM melts in a zone of free oxygen access near the ground surface [34]. In these conditions, the commonly predominant oxide and/or sulfide hosts of Fe, Co, Ni, Mn, and Zn give way to Fe^{3+}-bearing silicates (Ti-andradite and melilite).

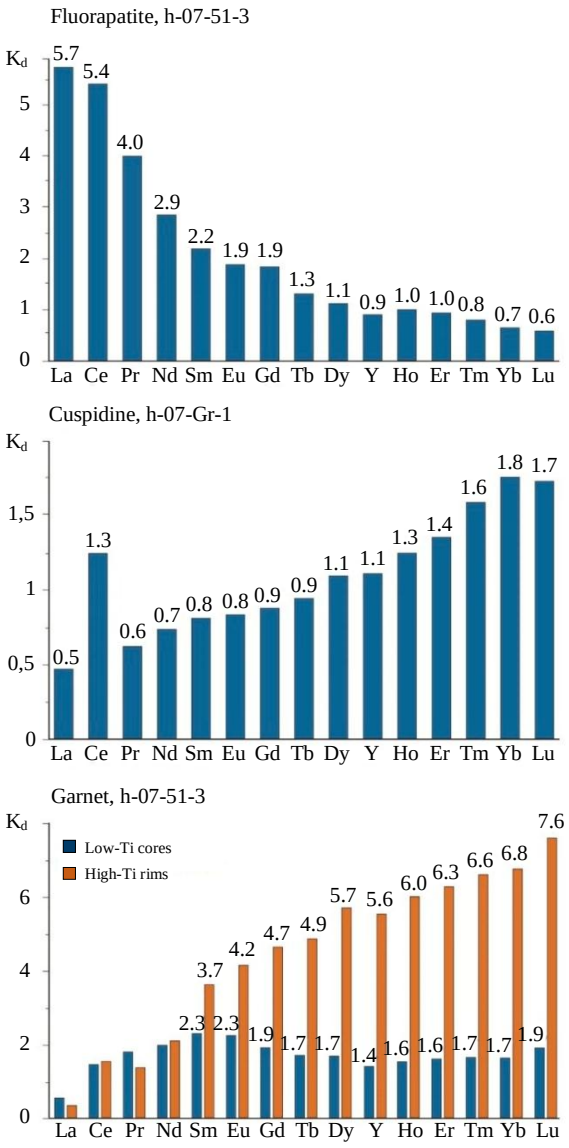

Fig.6. Partition coefficients of REE and Y in fluorapatite, cuspidine, and garnet from the Hatrurim Formation high-Ca paralava

As for large ion lithophile elements, the Hatrurim melilites store only Sr (K_d = 0.8-2.4) while Ba is mainly restricted to the rim (K_d = 0.3-1.7) at only $K_d < 0.1$ in the core. Sr can incorporate into the melilite structure also in igneous rocks from alkaline complexes. Most of Ba in these rocks resides in feldspar, though K_d of Ba exceeds 1 in a few analyses of melilite (Fig.7). The melilite structure is generally favorable for accommodating Ba at large cation sites, along with Fe, Co, Cu, and Mn at the T1 sites. At the time being, numerous Ba-analogs of akermanite ($BaMe^{2+}Si_2O_7$, where Me^{2+} = Mg, Co, Cu, Mn) have been synthesized [7]. The recent discovery of a natural Ba-bearing analog of melilite (bennesherite $Ba_2Fe^{2+}Si_2O_7$) was reported particularly from the Hatrurim Formation rocks [26].

The partition coefficients of REE we estimated for the melilite solid solutions from the Hatrurim paralava samples are below 0.1 and generally fit the ranges for melilite from igneous rocks (Fig.7). The K_d values for MREE and HREE decrease steadily till 0.01, while those for Y, HREE, as well as Zr and Hf, in melilite from paralava are likewise within the known values for magmatic melilite varying from 0.001 to 0.01 (Fig.7).

Garnets in the Hatrurim paralava store most of Ti, V, Cr, Zr, Hf, Nb, Ta, REE, Y, and Th. Andraditic cores contain more V, Nb, and Th than the high-Ti rims which show enrichment in HREE and Y, as well as in other HFSE (Sc, Zr, Hf, Ta) and Cr. The K_d coefficients approach 7 for Cr and

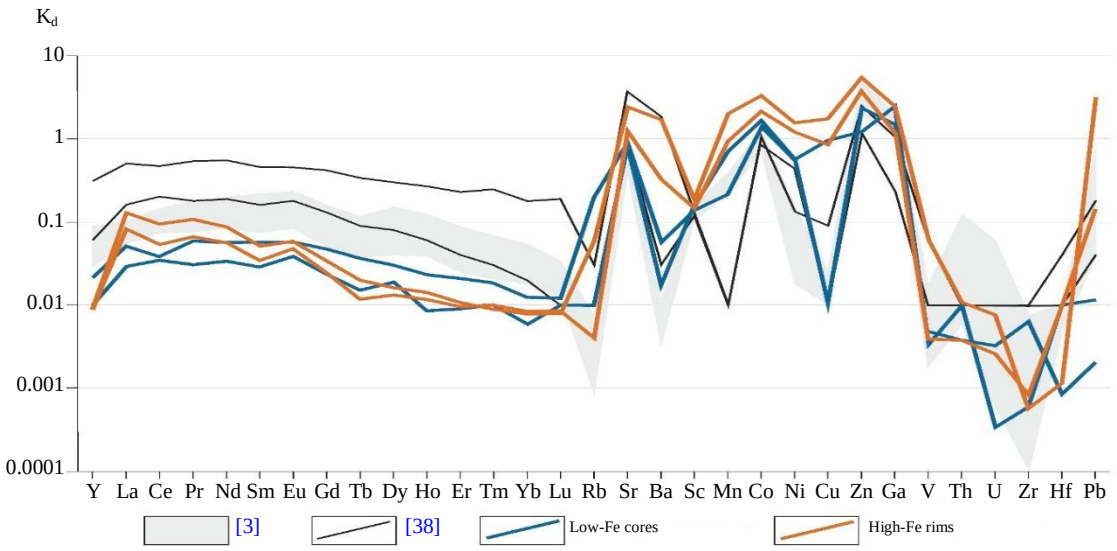

Fig.7. Partition coefficients of trace elements (including REE and Y) in melilite from the Hatrurim Formation high-Ca paralava, compared to published estimates [3, 38]. The curves represent K_d of specific analyzed paralava samples

Hf, 6 for Zr, 5 for Ti and Lu, 4 for other HREE, Sc, Ta, and Y, whereas those for U in garnet are as low as 0.1-0.35 (see Tables 2, 3, Supplements 1, 2).

High contents of uranium in the analyzed paralava samples (58.4 to 131 ppm) motivated the search for separate U phases. We found no Ca uranates, which are common to other Hatrurim CM rocks [33], but revealed extremely high concentrations of 2000 ppm U (K_d = 11.4) in large pure cuspidine grains ($Ca_4Si_2O_7F_2$). Cuspidine also competes with garnet in the accumulation of other HFSE (K_d from 2.5 to 4.0) and HREE (K_d up to 1.8) (see Tables 2, 3, Supplements 1, 2; Fig.5, 6). Cuspidine is enriched in HFSE apparently because these elements can easily form fluorine complexes [39]. The available data on the trace-element chemistry of cuspidine is very limited, but it is known to have structural affinity to Zr, Ce, La, Y, and Sr [40].

Conclusion

The patterns of element partitioning in main minerals of alkaline ultramafic rocks correspond to the trends of REE, Sr, Y, Zr, Hf, Nb, and Ta enrichment in the latest phases while the K_d values of these elements are far below 1 in the earliest phases of the crystallization sequence. This pattern was observed, for instance, in samples from the Khibiny alkaline ultramafic complex, with systematically high Nb, Ta, REE, Sr, and Y contents in all products of melts' differentiation [5]. We revealed a similar pattern in Ca-rich K-bearing Si-undersaturated combustion metamorphic melts. The contents of these elements are low ($K_d \leq 0.02$) in main rock-forming minerals from the Hatrurim Formation paralava samples (wollastonite, rankinite, and melilite solid solutions) which crystallized early from the CM melt, except for Sr and Ba stored in melilite.

As a result, the silicates that crystallized late from the Si-undersaturated and Ca-K-rich CM melts acquired times greater concentrations of K, Rb, Cs, Cr, V, Zr, Hf, Nb, Ta, Th, U, REE, and F, in the absence of the common hosts of incompatible elements (but for accessory fluorapatite). Such melts are compositionally favorable for crystallization of three rare minerals that can store the largest amounts of these elements: kalsilite, cuspidine, and Ti-andradite. Kalsilite becomes enriched in K (K_d = 24.5), Rb (K_d = 6.6), and Ba (K_d = 0.6), cuspidine hosts F (K_d = 20.8-23.8), Zr, Hf, Nb, Ta, U, Th, and HREE, while Ti-andradite accumulates Ti, V, Cr, Zr, Hf, Nb, Ta, REE, Y, and Th.

Melilite from the Hatrurim paralava samples bears signatures of isomorphic substitutions at all structural sites. Its late generations are especially prone to the formation of complex solid solutions. Melilites store Na (K_d = 6.6-7.3), Sr, and some Ba at the Ca site, Zn, Co, Ni, and Cu at the T1 site,

while Fe^{3+} and Ga occupy T2 (the assignment is by analogy with synthetic compounds). Although it is possible to synthesize REE-bearing compounds with a melilite-type structure, REE and other incompatible elements are reluctant to incorporate into melilite crystallized from natural CM melts. The K_d estimates of minor and trace elements in the Hatrurim melilites are consistent with earlier determinations for minerals from igneous alkaline complexes (Fig.7). These estimates can be used for quantitative reconstructions of element fractionation trends in Ca-rich alkaline melts.

The partitioning of elements between phases crystallized *in situ* from small batches of low-viscosity CM melts is mainly controlled by crystal chemistry of Ca silicates, aluminosilicates, and phosphates. The case we studied provides an idea of fractionation patterns for a large scope of trace elements during the crystallization of Si-undersaturated melts in the absence of phases that commonly host incompatible elements in igneous alkaline rocks.

Access to data

Additional materials are available at the following links:
Supplement 1, https://pmi.spmi.ru/pmi/article/download/16876/16670.
Supplement 2, https://pmi.spmi.ru/pmi/article/download/16876/16671.
Supplement 3, https://pmi.spmi.ru/pmi/article/download/16876/16672.
Supplement 4, https://pmi.spmi.ru/pmi/article/download/16876/16673.

We greatly appreciate the analytical support to this study by the Candidates of Geological and Mineralogical Sciences A.Ragozin, N.Karmanov, E.Nigmatulina; V.Danilovskaya and M.Khlestov from the Analytical Center for Multielement and Isotope Research at the V.S.Sobolev Institute of Geology and Mineralogy.

REFERENCES

1. Sukhanova K.G. Trace elements in the silicate minerals of the Borodino Meteorite (H5). *Journal of Mining Institute.* 2024. Vol. 265, p. 16-33.
2. Sukhanova K.G, Galankina O.L. Trace element composition of silicate minerals from Kunashak Meteorite (L6). *Journal of Mining Institute.* 2024. Vol. 270, p. 877-892.
3. Stoppa F., Jones A.P., Sharygin V. Nyerereite from carbonatite rocks at Vulture volcano: implications for mantle metasomatism and petrogenesis of alkali carbonate melts Research Article. *Central European Journal of Geosciences*. 2009. Vol. 1. Iss. 2, p. 131-151. DOI: 10.2478/v10085-009-0012-9
4. Arzamastsev A.A., Fedotov Zh.A., Arzamastseva L.V. Dike Magmatism in the Northeastern Fennoscandian Shield. St. Petersburg: Nauka, 2009, p. 383.
5. Arzamastsev A.A., Arzamastseva L.V. Geochemical Indicators of the Evolution of the Ultrabasic–Alkaline Series of Paleozoic Massifs of the Fennoscandian Shield. *Petrology*. 2013. Vol. 21. N 3, p. 249-279. DOI: 10.1134/S0869591113020021
6. Gusev N.I., Romanova L.Yu. Paleoproterozoic Saltakh Pluton, Anabar Shield: mineralogical composition, age and a geodynamic setting. *Journal of Mining Institute*. 2025. Vol. 272, p. 16-39.
7. Brooks K. Minerals explained 61: Melilites. *Geology Today*. 2021. Vol. 38. Iss. 1, p. 32-36. DOI: 10.1111/gto.12380
8. Fedorenko V., Czamanske G., Zenko T. et al. Field and Geochemical Studies of the Melilite-Bearing Arydzhangsky Suite, and an Overall Perspective on the Siberian Alkaline-Ultramafic Flood-Volcanic Rocks. *International Geology Review*. 2000. Vol. 42. Iss. 9, p. 769-804. DOI: 10.1080/00206810009465111
9. Wilkinson J.F.G., Stolz A.J. Low-pressure fractionation of strongly undersaturated alkaline ultrabasic magma: the olivine-melilite-nephelinite at Moiliili, Oahu, Hawaii. *Contributions to Mineralogy and Petrology*. 1983. Vol. 83. Iss. 3-4, p. 363-374. DOI: 10.1007/BF00371205
10. Cundari A., Ferguson A.K. Petrogenetic relationships between melilitite and lamproite. In the Roman Comagmatic Region: the lavas of S. Venanzo and Cupaello. *Contributions to Mineralogy and Petrology*. 1991. Vol. 107. Iss. 3, p. 343-357. DOI: 10.1007/BF00325103
11. Wiedenmann D., Keller J., Zaitsev A.N. Melilite-group minerals at Oldoinyo Lengai, Tanzania. *Lithos*. 2010. Vol. 118. Iss. 1-2, p. 112-118. DOI: 10.1016/j.lithos.2010.04.002
12. Melluso L., Srivastava R.K., Guarino V. et al. Mineral compositions and petrogenetic evolution of the ultramafic-alkaline – carbonatitic complex of Sung Valley, northeastern India. *The Canadian Mineralogist*. 2010. Vol. 48. N 1, p. 205-229. DOI: 10.3749/canmin.48.1.205
13. Ogorodova L.P., Gritsenko Y.D., Vigasina M.F. et al. Thermodynamic properties of natural melilites. *American Mineralogist*. 2018. Vol. 103. N 12, p. 1945-1952. DOI: 10.2138/am-2018-6475

14. MacPherson G.J. Calcium–Aluminum-rich Inclusions in Chondritic Meteorites. Treatise on Geochemistry. Elsevier, 2005. Vol. 1. Meteorites, Comets, and Planets, p. 201-246. DOI: 10.1016/B0-08-043751-6/01065-3

15. Ivanova M.A. Ca–Al-rich inclusions in carbonaceous chondrites: the oldest solar system objects. *Geochemistry International*. 2016. Vol. 54. N 5, p. 387-402. DOI: 10.1134/S0016702916050037

16. Rubin A.E., Chi Ma. Meteoritic minerals and their origins. *Geochemistry*. 2017. Vol. 77. Iss. 3, p. 325-385. DOI: 10.1016/j.chemer.2017.01.005

17. Asavin A.M. Partitioning of Trace Elements in the System 'Melt-Olivine-Ca Pyroxene' of Alkaline Melts: Evidence from Experiments and Field Data. Avtoref. dis. … kand. geol.-mineral. nauk. Irkutsk: Institut zemnoi kory SO RAN, 2016, p. 18.

18. Molendijk S.M., Namur O., Mason P.R.D. et al. Trace element partitioning in silica-undersaturated alkaline magmatic systems. *Geochimica et Cosmochimica Acta*. 2023. Vol. 346, p. 29-53. DOI: 10.1016/j.gca.2023.01.025

19. Pascal M.-L., Fonteilles M., Verkaeren J. et al. The melilite-bearing high-temperature skarns of the Apuseni Mountains, Carpathians, Romania. *The Canadian Mineralogist*. 2001. Vol. 39. N 5, p. 1405-1434. DOI: 10.2113/gscanmin.39.5.1405

20. Marincea Ş., Dumitraş D.-G., Ghineţ C. et al. Gehlenite from three occurrences of high-temperature skarns, Romania: new mineralogical data. *The Canadian Mineralogist*. 2011. Vol. 49. N 4, p. 1001-1014. DOI: 10.3749/canmin.49.4.1001

21. Pertsev N.N. High-Temperature Metamorphism and Metasomatism of Carbonate Rocks. Moscow: Nauka, 1977, p. 256.

22. Reverdatto V.V., Pertsev N.N., Korolyuk V.N. P_{CO_2}-*T*-Evolution and origin of zoning in melilite during the regressive stage of contact metamorphism in carbonate-bearing rocks. *Contributions to Mineralogy and Petrology*. 1979. Vol. 70. Iss. 2, p. 203-208. DOI: 10.1007/BF00374449

23. Sokol E.V., Kokh S.N., Polovykh A.S. et al. The Anakit contact aureole: spurrite–merwinite metamorphism and retrograde processes. *Russian Geology and Geophysics*. 2025. Vol. 66. N 11, p. 1446-1466. DOI: 10.2113/RGG20254887

24. Gross S. The Mineralogy of the Hatrurim Formation, Israel. Geological Survey of Israel, 1977. Bulletin 70, p. 80.

25. Grapes R. Pyrometamorphism. Springer, 2011, p. 376. DOI: 10.1007/978-3-642-15588-8

26. Krzątała A., Krüger B., Galuskina I. et al. Bennesherite, $Ba_2Fe^{2+}Si_2O_7$: A new melilite group mineral from the Hatrurim Basin, Negev Desert, Israel. *American Mineralogist*. 2022. Vol. 107. N 1, p. 138-146. DOI: 10.2138/am-2021-7747

27. Foit F.F., Hooper R.L., Rosenberg P.E. An unusual pyroxene, melilite, and iron oxide mineral assemblage in a coal-fire buchite from Buffalo, Wyoming. *American Mineralogist*. 1987. Vol. 72. N 1-2, p. 137-147.

28. Melluso L., Conticelli S., D'Antonio M. et al. Petrology and mineralogy of wollastonite- and melilite-bearing paralavas from the Central Apennines, Italy. *American Mineralogist*. 2003. Vol. 88. N 8-9, p. 1287-1299. DOI: 10.2138/am-2003-8-911

29. Peretyazhko I.S., Savina E.A. Melting Processes of Pelitic Rocks in Combustion Metamorphic Complexes of Mongolia: Mineral Chemistry, Raman Spectroscopy, Formation Conditions of Mullite, Silicate Spinel, Silica Polymorphs, and Cordierite-Group Minerals. *Geosciences*. 2023. Vol. 13. Iss. 12. N 377. DOI: 10.3390/geosciences13120377

30. Beckett J.R., Stolper E. The partitioning of Na between melilite and liquid: part I. the role of crystal chemistry and liquid composition. *Geochimica et Cosmochimica Acta*. 2000. Vol. 64. Iss. 14, p. 2509-2517. DOI: 10.1016/S0016-7037(00)00360-4

31. Warr L.N. IMA–CNMNC approved mineral symbols. *Mineralogical Magazine*. 2021. Vol. 85. Iss. 3, p. 291-320. DOI: 10.1180/mgm.2021.43

32. Seryotkin Yu.V., Sokol E.V., Kokh S.N. Natural pseudowollastonite: Crystal structure, associated minerals, and geological context. *Lithos*. 2012. Vol. 134-135, p. 75-90. DOI: 10.1016/j.lithos.2011.12.010

33. Sokol E.V., Kokh S.N., Sharygin V.V. et al. Mineralogical Diversity of Ca_2SiO_4-Bearing Combustion Metamorphic Rocks in the Hatrurim Basin: Implications for Storage and Partitioning of Elements in Oil Shale Clinkering. *Minerals*. 2019. Vol. 9. Iss. 8. N 465. DOI: 10.3390/min9080465

34. Sokol E., Novikov I., Zateeva S. et al. Combustion metamorphism in the Nabi Musa dome: new implications for a mud volcanic origin of the Mottled Zone, Dead Sea area. *Basin Research*. 2010. Vol. 22. Iss. 4, p. 414-438. DOI: 10.1111/j.1365-2117.2010.00462.x

35. Grew E.S., Locock A.J., Mills S.J. et al. Nomenclature of the garnet supergroup. *American Mineralogist*. 2013. Vol. 98. N 4, p. 785-811. DOI: 10.2138/am.2013.4201

36. Gee L.L., Sack R.O. Experimental Petrology of Melilite Nephelinites. *Journal of Petrology*. 1988. Vol. 29. Iss. 6, p. 1233-1255. DOI: 10.1093/petrology/29.6.1233

37. The Evolution of the Igneous Rocks. Fiftieth Anniversary Perspectives / Ed. by H.Yoder. Moscow: Mir, 1983, p. 528 (in Russian).

38. Arzamastsev A.A., Arzamastseva L.V., Bea F., Montero P. Trace Elements in Minerals as Indicators of the Evolution of Alkaline Ultrabasic Dike Series: LA-ICP-MS Data for the Magmatic Provinces of Northeastern Fennoscandia and Germany. *Petrology*. 2009. Vol. 17. N 1, p. 46-72. DOI: 10.1134/S0869591109010032

39. Gramaccioli C.M., Diella V., Demartin F. The formation of scandium minerals as an example of the role of complexes in the geochemistry of rare earths and HFS elements. *European Journal of Mineralogy*. 2000. Vol. 12. N 4, p. 795-808. DOI: 10.1127/ejm/12/4/0795

40. Bellezza M., Merlino S., Perchiazzi N. Chemical and structural study of the Zr, Ti-disilicates in the venanzite from Pian di Celle, Umbria, Italy. *European Journal of Mineralogy*. 2004. Vol. 16. N 6, p. 957-969. DOI: 10.1127/0935-1221/2004/0016-0957

***Authors*: Ella V. Sokol,** *Doctor of Geological and Mineralogical Sciences, Chief Researcher* (*V.S.Sobolev Institute of Geology and Mineralogy SB RAS, Novosibirsk, Russia*), *https://orcid.org/0000-0002-1130-6609*, **Anna S. Polovykh,** *Candidate of Geological and Mineralogical Sciences, Researcher* (*V.S.Sobolev Institute of Geology and Mineralogy SB RAS, Novosibirsk, Russia*), *devyatiyarova@igm.nsc.ru, https://orcid.org/0000-0003-0298-9185*, **Svetlana N. Kokh,** *Doctor of Geological and Mineralogical Sciences, Senior Researcher* (*V.S.Sobolev Institute of Geology and Mineralogy SB RAS, Novosibirsk, Russia*), *https://orcid.org/0000-0002-0264-7639*, **Ivan S. Karputin,** *Postgraduate Student, Research Engineer* (*V.S.Sobolev Institute of Geology and Mineralogy SB RAS, Novosibirsk, Russia*), *https://orcid.org/0009-0006-4651-1166*, **Olga A. Kozmenko,** *Lead Engineer* (*V.S.Sobolev Institute of Geology and Mineralogy SB RAS, Novosibirsk, Russia*), *https://orcid.org/0000-0003-4365-6483*.

The authors declare no conflict of interests.